UNIVERSITY OF MINNESOTA

Twin Cities Campus

Saint Anthony Falls Laboratory
Engineering, Environmental, Biological and Geophysical Fluid Dynamics

College of Science and Engineering

Mississippi River at 3rd Avenue S. E.
Minneapolis, MN 55414

Dept. Main Office: 612-624-4363
Fax: 612-624-4398

Project Title: Virtual Wind Simulator with Advanced Control & Aeroelastic Model for Improving the Operation of Wind Farms

Contract Number: RD4-13 **Milestone Number**: 4 **Report Date**: 12/8/2017

Principal Investigator: Fotis Sotiropoulos
(631) 632-8380

Contract Contact: Bridget Foss
(612) 624-5571

Congressional District: (Corporate office) Minnesota 5^{th}

Congressional District: (Project location) Minnesota 5^{th}

MILESTONE REPORT

Executive Summary: The goal for this project is to develop, demonstrate and transfer into practice an industry-leading numerical simulation model for optimization of performance, financial decision making, and operational planning of existing and newly planned wind energy plants. This project will leverage the previously completed Cycle 3 RDF project through which the first version of the Virtual Wind Simulator software (VWiS) was developed and validated. We will extend the capabilities of this first generation modeling tool to include the ability to simulate aeroelastic loading of the blades and incorporate current industry standards and advanced turbine control methods and technologies and we will demonstrate these capabilities via comparisons with data from utility-scale wind turbines and farms. The resulting VWiS+ modeling tool will thus be able to be used in practice to improve wind farm performance and reduce operational costs.

As planned, during this reporting period (monthly) activities have been carried out to address the following objectives:

1. Design and implementation of individual blade pitch control for load migration;
2. XCEL Energy wind farm simulations;
3. Simulation of EOLOS turbine under different operating conditions.

Project funding provided by customers of Xcel Energy through a grant from the Renewable Development Fund.

Technical Progress:

1 Progress 1: Implementation of individual blade pitch control for load migration

1.1 Firmware Implementation

With the hardware installed on the turbine, individual blade-pitch controllers can be implemented on the turbine control unit (TCU) by transferring the Matlab/Simulink controller model to C code and incorporating the code into the control firmware. Here, both the individual blade-pitch controller with a decoupled integral compensator and the H_∞ controller are implemented on the TCU for a comprehensive comparison in future field tests.

As safety is the primary concern in the development and implementation of individual blade-pitch controllers, the updated firmware is first tested in software only simulations. Specifically, individual blade-pitch commands generated from blade moment measurements are not injected to blade-pitch actuators but only collected along with blade moment measurements. These commands are compared with Matlab/Simulink generated commands using the collected blade moment measurements. The results show that individual blade-pitch controllers implemented on the firmware behave exactly the same as the designed controllers in Matlab/Simulink.

In the second step, individual blade-pitch controllers are included in the feedback loop of the control firmware. In other words, individual blade-pitch commands are injected to blade-pitch actuators. For safety concerns, linear ON/OFF switches are proposed in individual blade-pitch controllers to provide a smooth transition between individual and collective blade-pitch controls. The linear ON/OFF switch generates a linearly time dependent increasing/decreasing gain in the range of 0 to 1 on individual blade-pitch commands when the ON/OFF signal is provided. The switching time between ON and OFF status is $0.1\,s$, which should be fast enough in emergent situations. Theoretical analysis shows that the closed loop system with a specific gain between 0 to 1 is stable. Stability of the system when the gain is varying during the switching process has also been verified in FAST simulations. Therefore, the linear ON/OFF switches are implemented in the firmware as parts of the individual blade-pitch controllers. Initial tests on the turbine show that the switch provides a fast and smooth transition between individual and collective blade-pitch controls. The tests also show that the individual pitch controllers operate normally without introducing unsafe conditions or interfere in safe operations. Therefore, both two individual blade-pitch controllers are ready for long term field tests to validate the load reduction performance.

1.2 Initial Test Plan

After the successful implementation of the individual blade-pitch controllers on the TCU, an initial test plan is proposed here to guide the coming field tests and ensure a comprehensive evaluation of the control algorithms. In the stage of firmware implementation, the turbine is closely monitored and various intermediate states of the turbine are recorded for analysis. In the long term field tests, however, these states are considered redundant and therefore removed from the list of signals.

Instead, more sensor measurements are included here, such as tower, nacelle and rotor shaft loads, which will be used to fully evaluate the load reduction performance using the individual blade-pitch controls. As a reference, Table 1.1 lists all required signals to be collected for field tests.

It is proposed that a typical test cycle lasts for $30\,min$. The test cycle switches among collective blade-pitch control, individual blade-pitch control with decoupled integral compensator and the H_∞ control. Therefore, each control algorithm runs for $10\,min$. The experiment data as listed in Table 1.1 will be recorded and saved for later analysis. At the same time, the met-tower data of the wind speed measurements will be collected along with the experiment data file. The met-tower data will be used in post analysis to identify wind conditions (average wind speed, turbulence intensity and wind shear) and categorize the experiment data files. Table 1.2 shows details on how to categorize the experiment data based on wind conditions, which will be helpful to fully evaluate the individual blade-pitch controls.

Table 1.1: Signals to be collected for field tests.

No.	Signal
0	Time
1	TCU State
2	DelKw
3	Real Power
4	Generator Speed
5	Wind Speed
6	Eol Enable
7	IPC Gain Setting
8	Azimuth Angle
9	Blade 1 Out of Plane Moment
10	Blade 2 Out of Plane Moment
11	Blade 3 Out of Plane Moment
12	Blade 1 In Plane Moment
13	Blade 2 In Plane Moment
14	Blade 3 In Plane Moment
15	Blade 1 Pitch Demand
16	Blade 2 Pitch Demand
17	Blade 3 Pitch Demand
18	Collective Pitch Demand
19	Nacelle Yaw Moment
20	Nacelle Pitch Moment
21	Shaft Bending Moment (y-axis)
22	Shaft Bending Moment (z-axis)

Table 1.2: Test Matrix

		Capture matrix for IBC Testing								
			Wind Speed (m/s)							
IBC System State	Wind Shear	Turbulence Intensity (%)	>9 to 11	>11 to 13	>13 to 15	>15 to 17	>17 to 19	>19 to 21	>21 to 23	>23 to 25
IBC "OFF"	<.10	<7%								
		7% to 15%								
		>15%								
	>0.10 & <0.20	<7%								
		7% to 15%								
		>15%								
	>0.20	<7%								
		7% to 15%								
		>15%								
	Extreme yaw error									
IBC "ON"	<.10	<7%								
		7% to 15%								
		>15%								
	>0.10 & <0.20	<7%								
		7% to 15%								
		>15%								
	>0.20	<7%								
		7% to 15%								
		>15%								
	Extreme yaw error									
Minimum number of 10 minute time series files at each combination of wind speed and wind shear			12	12	10	6	6	4	2	0

1.3 Summary of progress 1

The controller using a multivariable individual blade-pitch control law to simultaneously reduce structural loads on the rotating and non-rotating parts of a wind turbine, which has been verified in extensive simulations, has been successfully implemented on the 2.5 MW Clipper Liberty research turbine operated by the University of Minnesota. An initial plan has also been proposed for field tests in the coming future.

2 Progress 2: Pleasant Valley wind farm simulation

Simulation of Pleasant Valley wind farm was carried out using the developed code Virtual Flow Simulator (VFS-Wind) (which was called Virtual Wind Simulator (VWiS) for the previous version of the code). In this wind farm simulation, Large-eddy simulation with the dynamic subgrid scale model is employed for simulating the atmospheric boundary layer flows. Actuator line model is employed for modeling turbine blades. The turbine nacelle is modeled by simply extending the actuator lines to the center.

2.1 Computational setup

The lengths of the computational domain are $L_x \times L_y \times L_z = 22.5km \times 14.5km \times 1km$ with the number of grids nodes $N_x \times N_y \times N_z = 1126 \times 1488 \times 152$ in the downwind, crosswind and vertical directions, respectively. In the wind turbine region, the grid spacings are $\Delta x = \Delta y = 10\ m$ and $\Delta z = 2\ m$. The height of the domain represent the thickness of atmospheric boundary layer, which is 1 km in the present simulations. In the Pleasant Valley wind farm, there are 100 Vestas V100 2.0 WM turbines. The diameter of the turbine rotor is 100 m. The hub height of the turbine is 95 m. In the simulation, wind blows from the north. The tip-speed ratios, which are different for different turbines, are around 8 9. The terrain in the Pleasant Valley wind farm is fairly flat as shown in Fig. 2.1. In the simulation, the terrain was simply assumed to be flat. Two simulations have been carried out: 1) one precursor simulation with periodic boundary conditions in the horizontal directions for providing inflow for the wind farm simulation; and 2) the wind farm simulation.

2.2 Results

Figure 2.2 shows the instantaneous downwind velocity contours on a horizontal plane located at turbine hub height from precursor inflow simulation. This figure shows the spatial fluctuations in the atmospheric turbulent flows. It is also observed those high-speed and low-speed streaks, with the crosswind length scale in the order boundary layer thickness (1 km) and much larger downwind length scale (10 km or even larger). Figure 2.3 shows the mean downwind velocity and turbulence intensities of the incoming atmospheric turbulent flow. As seen, the mean downwind velocity computed from the simulation agree well with the logarithmic law. In Figure 2.3(a), it is seen that very high turbulence intensities ($\sigma_u/u^* \approx= 2.1$, $\sigma_v/u^* \approx= 1.4$ and $\sigma_w/u^* \approx= 1.4$, where u^* is the

Figure 2.1: Google map of Pleasant Valley wind farm.

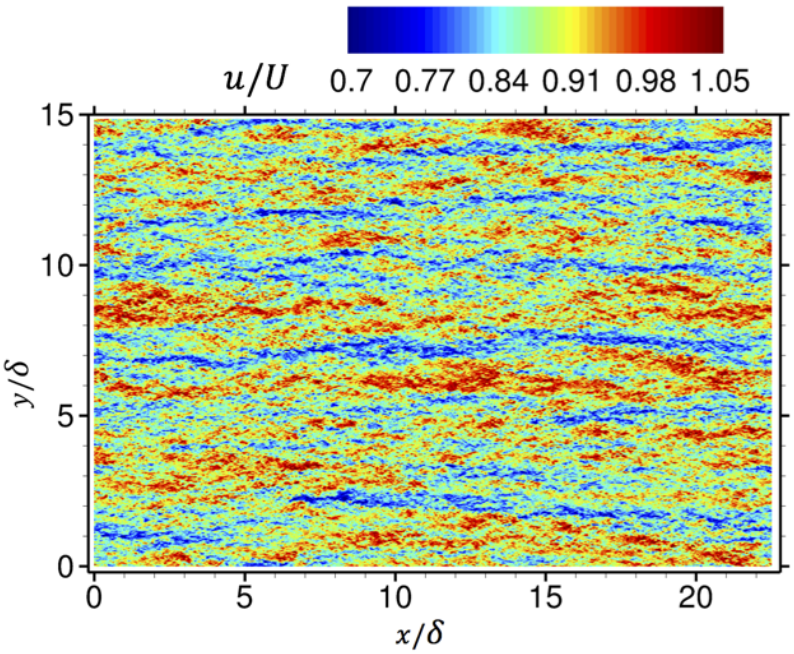

Figure 2.2: Contours of instantaneous downwind velocity from the precursor inflow simulation.

friction velocity) exist the turbine region, which highlights the importance of considering incoming turbulence in wind farm design and wind turbine operations.

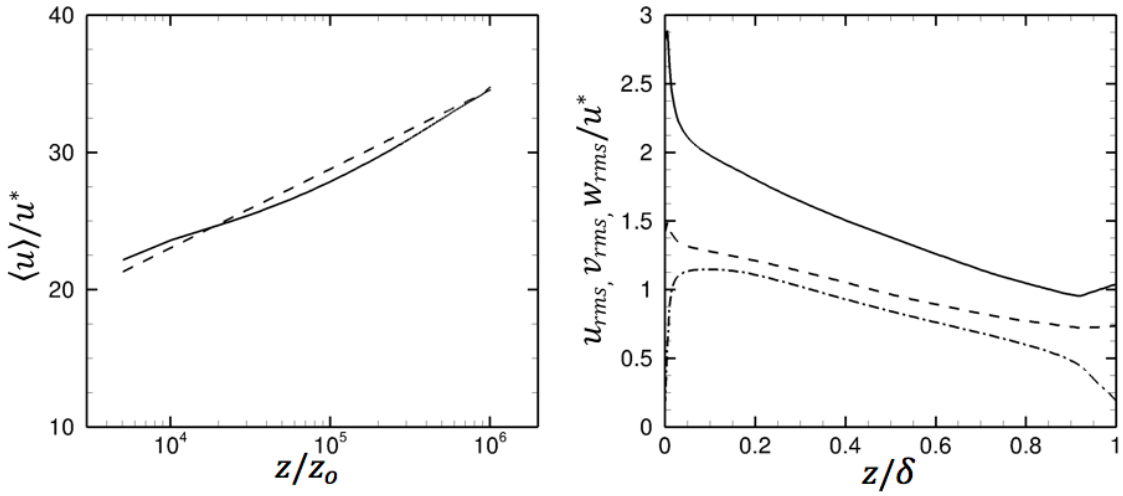

Figure 2.3: (a) Mean downwind velocity and (b) turbulence intensities of incoming atmospheric turbulent flow. In (a), the solid line and dashed line show the computed results and logarithmic low ($\frac{\langle u \rangle}{u^*} = \frac{1}{\kappa} \ln \frac{z}{z_0}$, where $z_0 = 0.005m$ is the surface roughness height.). In (b) the solid, dashed and dash-dot lines represent the downwind, spanwise, and vertical turbulence intensities (σ_u / u^*, σ_v / u^* and σ_w / u^*), respectively.

Figure 2.4 shows contours of instantaneous downwind velocity on the horizontal plane located at turbine hub height from the wind farm simulation. It is seen in Figure 2.4(e) that not every nearby turbine has a strong interaction with the surrounding turbines because of the relatively irregular and sparse turbine layout of the wind farm. Figures 2.4 (a) and (d) show the scenario that each turbine wake evolves almost individually without interacting without the adjacent turbine wakes in the crosswind and the upwind turbine wakes have negligible or relatively small effects on the downwind turbines. In Figure 2.4 (b), it is seen that two adjacent wakes merging with each other and strongly influencing the downwind turbines. Figure 2.4 (c) shows a super wake formed by more than three turbine wakes, which persists very far in the downwind direction.

Figure 2.5 shows the comparison of the computed results with SODAR measurements. It is seen that the computed and measured mean downwind velocity agree well with each other at S3, S4, S6 locations. At S1 location, both measurements and simulations show the wake from the upwind turbine. However, the velocity deficit from the measurements is significantly smaller. This is probably because of the averaging procedure when processing the data, in which the velocity was averaged over a range of wind directions. In the simulation, on the other hand, only a single wind direction was considered. At S2 and S5 locations, turbine wakes are observed from the simulation results, which do not exist in the measurements. It is probably because of the relatively small amount

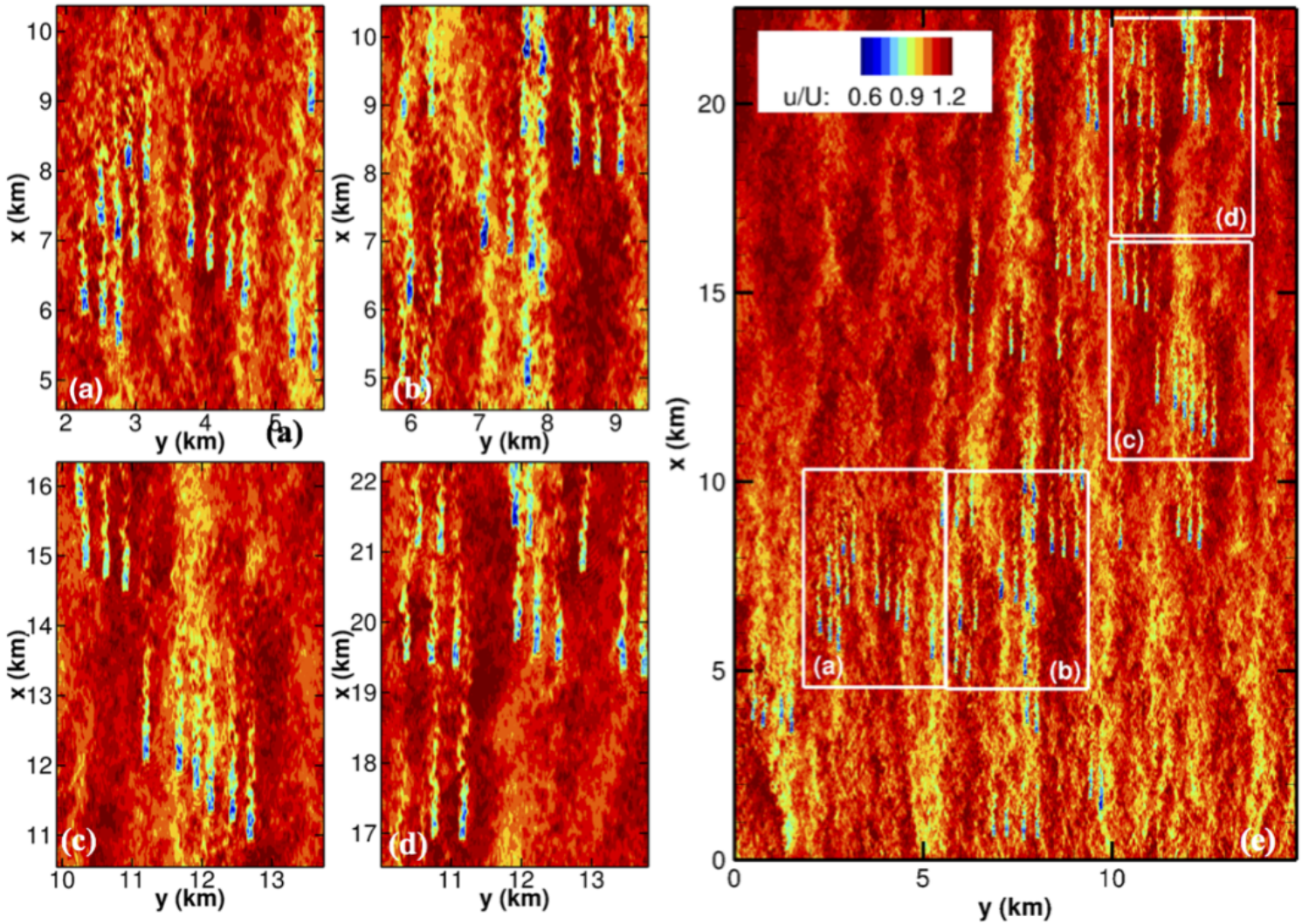

Figure 2.4: Contours of instantaneous downwind velocity on the horizontal plane located at turbine hub height in (a), (b), (c) and (d) for some enlarged regions as indicated in (e) flowfield of the whole wind farm. In the figure, the wind blows from right to left.

of samples available in the measurements, which do not include wake measurements.

2.3 Summary of progress 2

Simulations of the XCEL Energy Pleasant Valley wind farm have been carried out. Computed results show acceptable agreements with the measurements considering the large uncertainties in the field measurements. Simulations of some interested regions with different turbine controls will be carried out in the future work to evaluate the effects of advanced turbine control algorithm on load reduction and overall performance of the wind farm.

3 Progress 3: EOLOS turbine simulation

3.1 Introduction

Conventional turbine control algorithm aims at maximizing the power output of each individual turbine. This, however, often results suboptimal performance of the whole wind farm. To optimize the performance of the whole wind farm, advanced wind farm control strategies, such as coordinated turbine control through axial induction factor and yaw-based wake redirection method, have been developed. For instance, Fleming et al. [2] studied three different wake redirection methods including yaw-based, tilt-based and IPC (individual pitch control)-based methods for improving the wind farm overall performance using large-eddy simulation with actuator line model for turbine blades. Using large-eddy simulation, Annoni et al. [1] showed that the performance of a turbine array can be improved by derating the upwind turbines through axial induction factor control. The major difficulty to develop an effective wind farm control models originates from the limited knowledge of turbine wake dynamics under realistic atmospheric conditions and site-specific complex terrains. The objective of this work is to systematically investigate the wake characteristics of a turbine operating under suboptimal conditions and the potential for improving wind farm performance.

3.2 Computational setup

The lengths of the computational domain are $L_x \times L_y \times L_z = 22D \times 10D \times 10D$ with the number of grids nodes $N_x \times N_y \times N_z = 433 \times 339 \times 152$ in the downwind, crosswind and vertical directions, respectively. In the wind turbine region, the grid spacings are $\Delta x = \Delta y = \Delta z = D/48$. The height of the domain represent the thickness of atmospheric boundary layer, which is 1 km in the present simulations. Four different tip-speed ratios, i.e. $\lambda = \Omega R/U_h = 6.8, 7.8, 8.8, 9.3$ (where Ω is the rotor rotational speed, $R = 48m$ is the rotor radius and U_h is incoming downwind velocity at turbine hub height), were simulated to represent four different operating conditions. The case with $\lambda = 7.8$ represents the condition close to optimal. The size of time step is $\Delta t = 0.002U/D$, which is the same for all the cases. The flowfields were averaged for more than 900 rotor revolutions after fully developed.

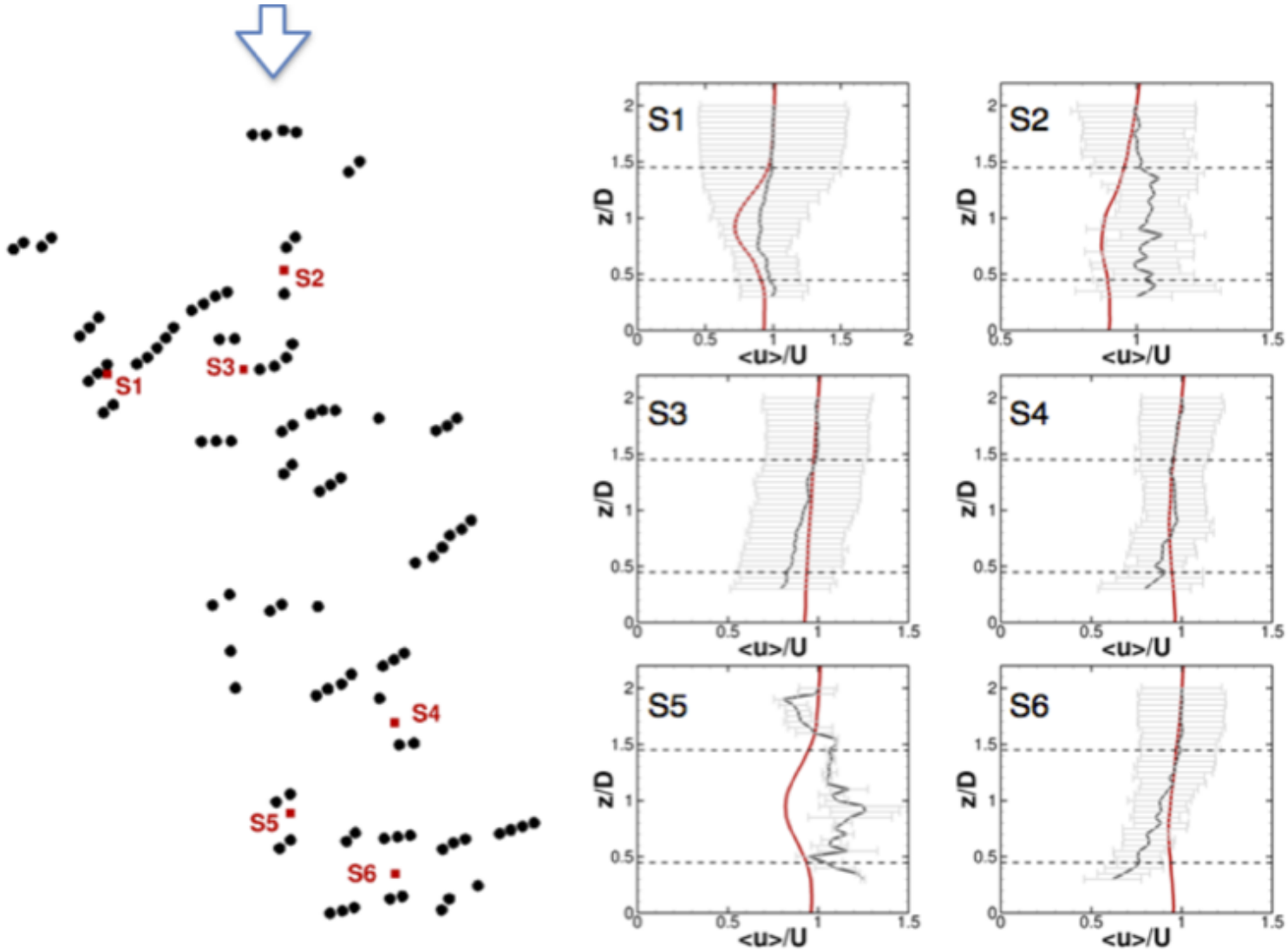

Figure 2.5: Comparison of the computed mean downwind velocity with SODAR measurements. Left: turbine locations (black dots) and SODAR locations (red dots); Right: red lines and grey lines with error bars represent the computed and measured mean downwind velocities, respectively.

3.3 Results

Figure 3.1(a) shows the variation of time and disk-averaged downwind velocity at different downwind locations. As seen, increasing the tip-speed ratio decrease the downwind velocity until about $5D$ turbine downwind. Decreasing the tip-speed ratio, on the other hand, increases the downwind velocity at almost all considered downwind locations. From this observation, we can anticipate that lowering the tip-speed ratio of the upwind turbine may increase the power of two turbines comparing to the situation when the upwind turbine operating optimally. To evaluate this, we hypothetically placing a turbine at different downwind locations for different tip-speed ratio cases. It is seen in Figure3.1(b) that significant increase in power production from two turbines appears when the downwind turbine is located within about $7D$ turbine downwind. Figure 3.2 show the

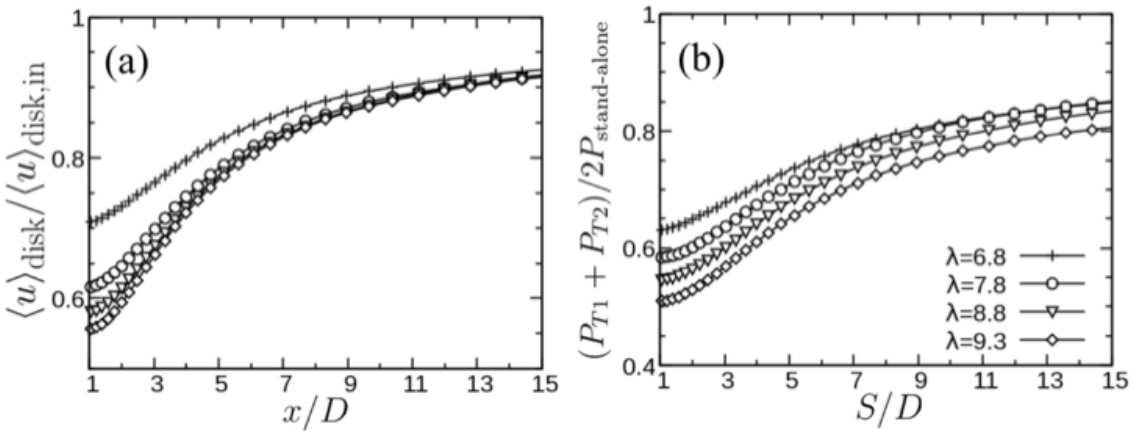

Figure 3.1: (a) Variation of time and disk-averaged downwind velocity at different downwind locations. (b) Ratio of power from two turbines with the downwind turbine placed hypothetically at different downwind locations with power from two stand-alone turbines.

downwind variation of disk-averaged turbulence intensity (upper row) and maximum turbulence intensity within the disk (lower row) for the three components of turbulence intensities. As seen, increasing tip-speed ratio increases the different components of turbulence intensities at different downwind locations. Decreasing tip-speed ratio decrease the turbulence intensities except for the disk-averaged downwind component turbulent intensity in the near wake (x<2D) where increase is observed.

The instantaneous downwind velocity fields for the cases with different tip-speed ratios are shown in Figure 3.3. As seen in the near wake (until $9D$), the cases with higher tip-speed ratios show slightly longer wakes as expected. Despite differences in small structures, similarity in the large-scale structures is observed at different downwind locations. To examine such similarity, we show the power spectral density in Figure. 3.4. As seen, a significant amount of energy exist at a very low frequency with $fU_h/D \approx 0.01$, which comes from the inflow as it exists at all downwind locations. Loss of energy at this low frequency is observed in turbine wake. As moving downwind,

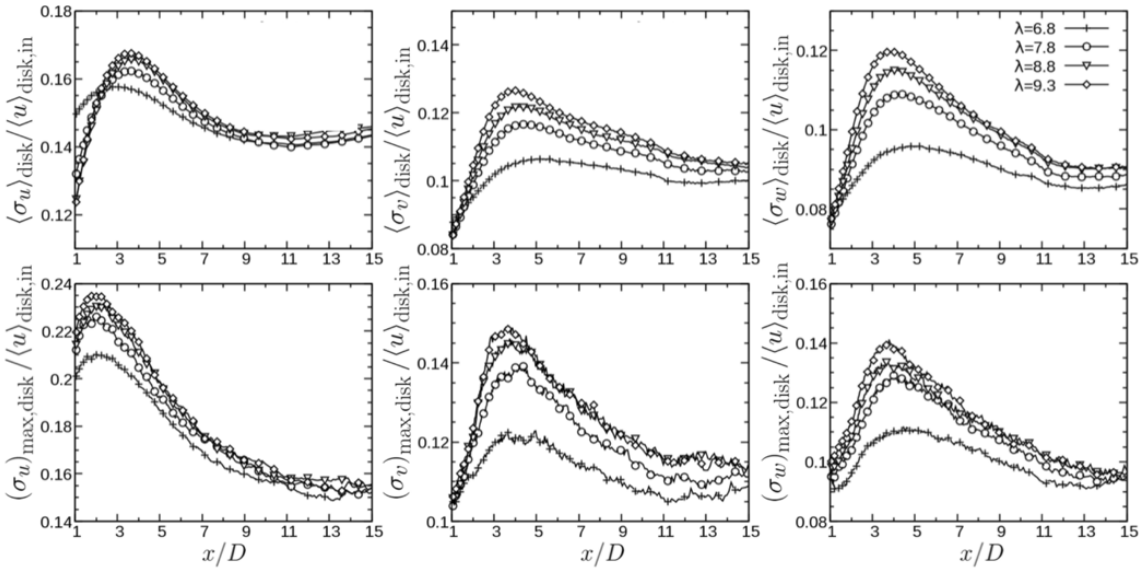

Figure 3.2: Downwind variation of disk-averaged turbulence intensity (upper row) and maximum turbulence intensity within the disk (lower row) for the three components of turbulence intensities, i.e., σ_u, σ_v and σ_w for downwind, crosswind and vertical directions, respectively.

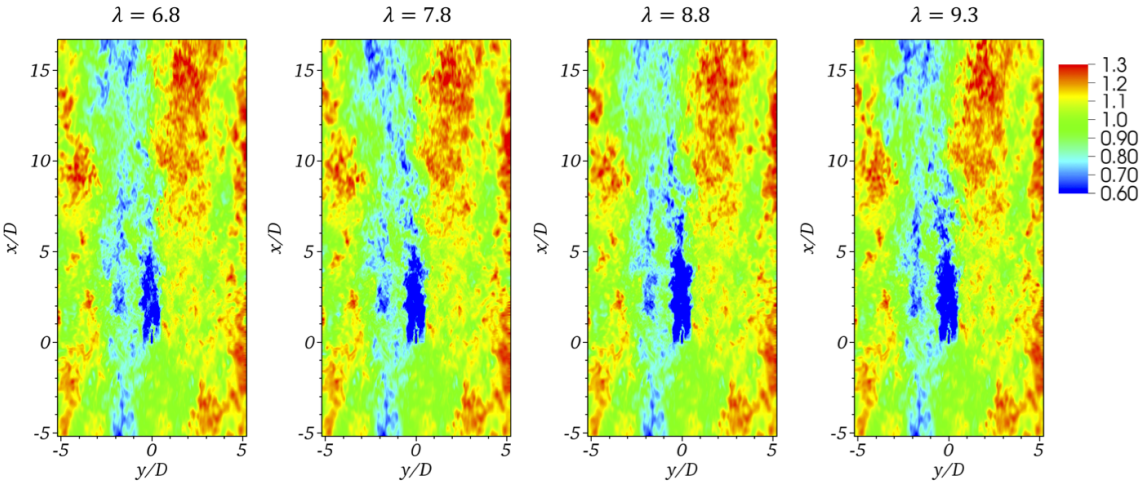

Figure 3.3: (a) Averaged incoming wind speed and (b) turbulence intensities of the incoming flow.

the energy at this low frequency is gradually recovered. Higher frequency for wake meandering at about $fU_h/D \approx 0.2$ is also observed. To observe this wake meandering frequency more clearly,

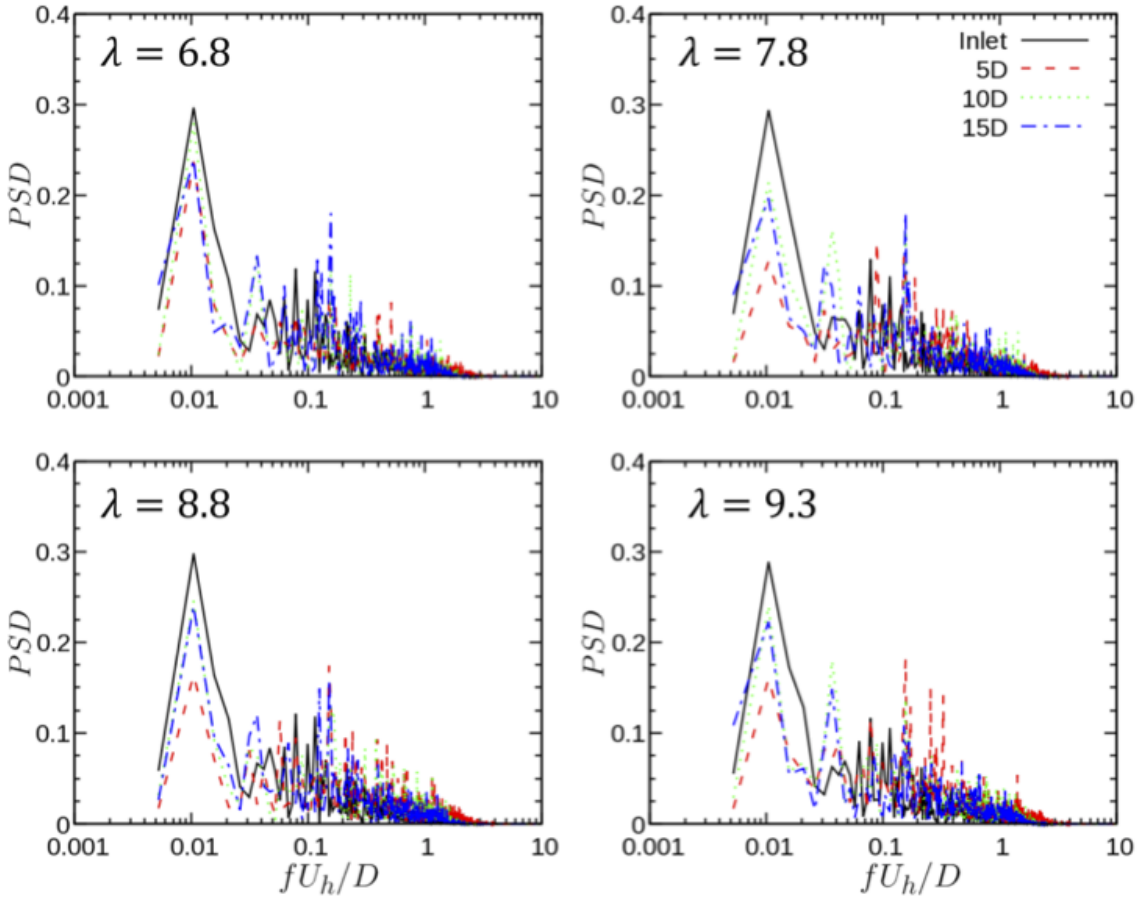

Figure 3.4: Power spectral density showing the dominant frequency from incoming wind persists at different downwind locations.

we show the power spectral density averaged over different periods in Figure 3.5. As seen this frequency is between $0.1 \sim 0.2$. It is almost the same for different cases. Such frequency exists at different downwind locations, $5D$, $10D$ and $15D$. The downwind variations of the energy at the meandering frequency are different for different cases.

To further analyze the large coherent structures in turbine wake, proper orthogonal decomposition (POD) is carried for different operating conditions. Figure 3.6 shows the POD spectrum for different cases. It is seen that only two POD modes are significantly affected in the turbine wake, one is the first mode with $k = 0$, the other one is the 5th mode at $k = 4$. These two modes with big differences between different cases are then shown in Figure 3.7.

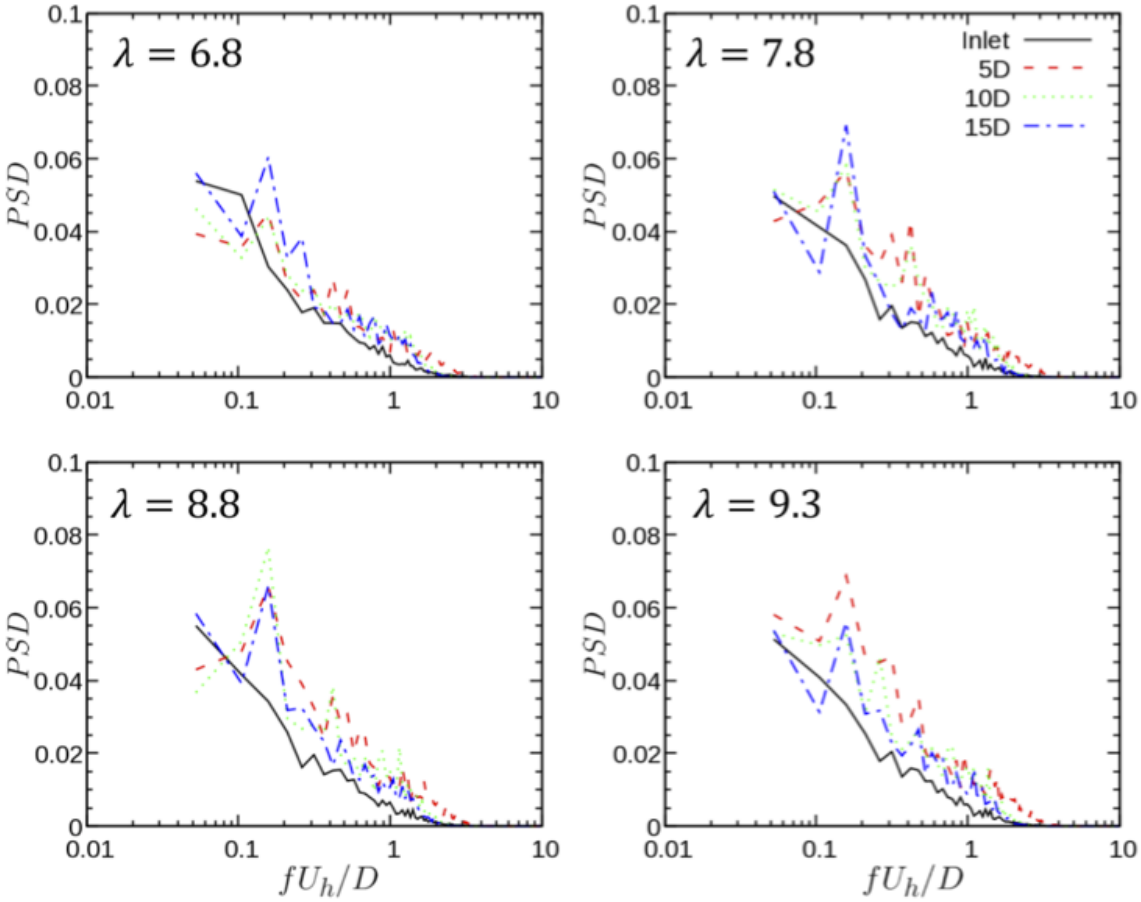

Figure 3.5: Power spectral density showing the wake meandering frequency for different operating conditions.

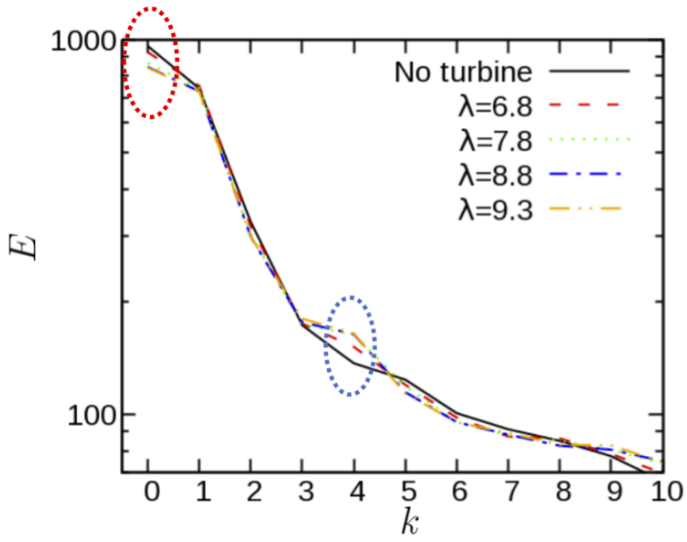

Figure 3.6: POD spectrum for different cases.

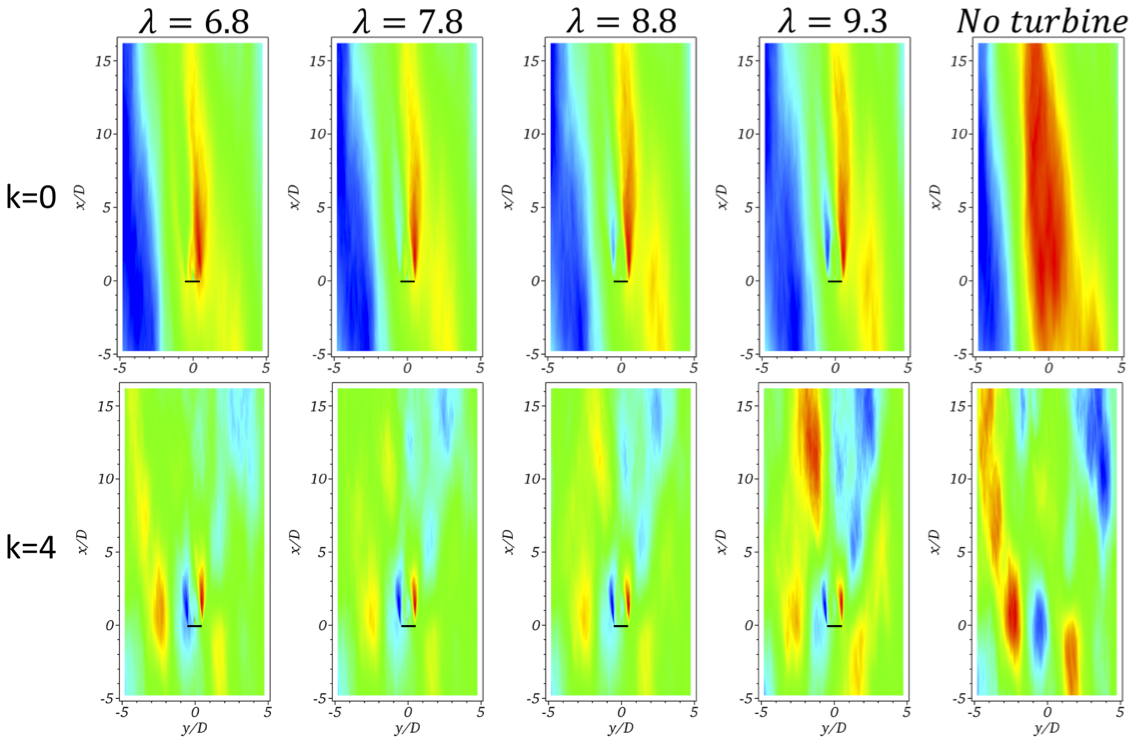

Figure 3.7: POD modes at $k = 0$ and $k = 4$ for different cases.

3.4 Summary of progress 3

We investigated the wake dynamics of the EOLOS turbine at different operating conditions by varying tip-speed ratios in the simulations. From these simulations, we see potential increase in power production and decrease in blade load by derating the upwind turbine through lowering tip-speed ratio. The considered cases have significantly different power and thrust coefficients. However, the similarity in wake meandering and the dominance of the large-scale turbulent flow are observed at different downwind locations.

References

[1] ANNONI, J., GEBRAAD, P. M., SCHOLBROCK, A. K., FLEMING, P. A., AND WINGERDEN, J.-W. V. Analysis of axial-induction-based wind plant control using an engineering and a high-order wind plant model. *Wind Energy 19*, 6 (2016), 1135–1150.

[2] FLEMING, P. A., GEBRAAD, P. M., LEE, S., VAN WINGERDEN, J.-W., JOHNSON, K., CHURCHFIELD, M., MICHALAKES, J., SPALART, P., AND MORIARTY, P. Evaluating techniques for redirecting turbine wakes using sowfa. *Renewable Energy 70* (2014), 211–218.

Project Status : This project is on schedule and within budget.